Milli-Hertz Frequency Tuning Architecture Toward High Repeatable Micromachined Axi-Symmetry Gyroscopes

Chong Li, *Member, IEEE*, Yuchen Wang, *Student Member, IEEE*, Choon Ki Ahn, *Senior Member, IEEE*, Chengxi Zhang, *Member, IEEE*, and Bo Wang, *Graduate Student Member, IEEE*

***Abstract*—Axi-symmetry micro gyroscopes are increasingly popular for their ultrahigh measurement sensitivity. However, a side effect is the bias repeatability problem. In this article, we propose and demonstrate an ultraprecise frequency tuning solution to achieve state-of-the-art repeatability performance. The gyroscope dynamics are first analyzed and the major error source is confirmed as the frequency split. Then, an advanced frequency tracker and a precision tuning architecture are developed to improve the bias repeatability. The experimental results prove that the frequency tracker can identify the frequency splits at the mHz level. Consequently, a state-of-the-art turn-ON to turn-ON bias repeatability of 3.6°/h is conducted that shows orders of magnitude better than conventional solutions.**

***Index Terms*—Bias repeatability, frequency tuning, inertial measurement unit (IMU), inertial sensors, MEMS gyroscope.**

NOMENCLATURE

x, y	Displacements of the two modes.
m	Effective mass.
c_x, c_y	Damper coefficients.
k_x, k_y	Spring coefficients.
F_x, F_y	Electrostatic drive forces.
Ω_z	Physical rotation in the Z axis.
k_{xy}, k_{yx}	Stiffness coupling coefficients.
c_{xy}, c_{yx}	Damper coupling coefficients.
ω_x, ω_y	Resonant frequencies of the two modes.
Q_x, Q_y	Quality factors of the two modes.
ω_{xy}, ω_{yx}	Cross coupling frequency.
ρ_{xy}, ρ_{yx}	Cross coupling damper.
$\Delta\omega$	Frequency split.
ψ	Phase shift between the excitation and output signals.
$f(t)$	Excitation frequency.
γ	Time delay coefficient.
ω_δ	Equivalent disturbance from the variation of ω_x.
$e(t)$	Instaneous controller.
k_1, k_2	Control parameters of OLC.
τ	Learning interval.
$\tilde{f}$	Learning difference.
k_p, k_i	Control parameters of PI.
$z(t), V, \kappa_1, \kappa_2, \mu, \Pi$	Intermediate variables.

Manuscript received 11 February 2022; revised 23 May 2022 and 19 June 2022; accepted 13 July 2022. Date of publication 26 July 2022; date of current version 23 January 2023. This work was supported in part by the National Natural Science Foundation of China under Grants 62171420 and 62003112, in part by the Natural Science Foundation of Shandong Province under Grant ZR201910230031, and in part by the National Research Foundation of Korea (NRF) grant funded in part by the Korea government (Ministry of Science and ICT) under Grant NRF-2020R1A2C1005449. *(Corresponding author: Chong Li.)*

Chong Li and Yuchen Wang are with the Department of Automation and Measurement, Ocean University of China, Qingdao 266100, China (e-mail: lichong7332@ouc.edu.cn; wyc@stu.ouc.edu.cn).

Choon Ki Ahn is with the School of Electrical Engineering, Korea University, Seoul 136-701, South Korea (e-mail: hironaka@korea.ac.kr).

Chengxi Zhang is with the School of Electronic and Information Engineering, Harbin Institute of Technology, Shenzhen 518055, China (e-mail: zhangchengxi@hit.edu.cn).

Bo Wang is with the Department of Mechanical Engineering, Villanova University, Villanova, PA 19085 USA (e-mail: bwang6@villanova.edu).

Color versions of one or more figures in this article are available at https://doi.org/10.1109/TIE.2022.3192672.

Digital Object Identifier 10.1109/TIE.2022.3192672

I. INTRODUCTION

AXI-symmetry microelectromechanical system (MEMS) gyroscopes are increasingly important in both industry and academia [1] and [2]. The commonly used design includes rings [3], solid disks [4], honeycomb [5], and hemispherical shells[6]. Compared to the traditional tuning fork and butterfly shapes, the symmetry design results in a mode-matched operation[7]. These architectures cooperated with ultra high-quality (Q) factor $>$ 50 000 can significantly improve the physical rate sensitivities [8], [9]. Recent reports prove that axi-symmetry gyroscopes are about to provide a 0.01°/h bias instability level performance [10]. If miniaturized and cheap microgyroscopes can replace expensive optical fiber gyroscopes, there will be a great impact on the micropositioning, navigation, and timing (mPNT) systems [11].

Though we are on the eve of the mPNT revolution, most axi-symmetry gyroscopes are laboratory samples and their robustness and reliability remain as an open issue. More specifically, their repeatability and environmental dependency are not fully evaluated yet. To address these concerns, the first clue of course would be fabricating high-quality microdevices by optimizing mechanical design, alternating packaging solutions, and improving microfabrication processes [12] and [13]. Turn-ON to turn-ON bias repeatability is one of the crucial issues in mPNT and inertial measurement systems, since the turned-ON random output error greatly affects the positioning accuracy [14]. Unlike the conventional tuning fork/mass-spring-damper structures, axi-symmetry gyroscopes are more sensitive to mechanical deformations and have much weaker bias repeatability [15]–[17]. Few research works about this issue have been reported, and one of the recent reports demonstrated 50°/h bias repeatability level performance in the application of compensated inertial measurement units [18].

The frequency split is considered as the main contributor to the repeatability problem for axi-symmetry gyroscope systems [19]. It is even more serious for the commonly used high-Q designs—a small amount of frequency split/anisoelasticity leads to apparent asymmetry, which hurts the bias repeatability. The frequency split variations are making this issue even worse, which is caused by the material's nonidealities [8]. Toward reliable and product-level axi-symmetry gyroscopes, the demands on practical mode matching techniques have been never stronger. The first barrier would be the resonant frequency detection methodologies. A quadrature test signal injection mode matching method was proposed for dual/quad mass gyroscopes in [20]. Later, a dual mode architecture with automatic mode matching was investigated for microbulk-acoustic-wave gyroscopes in [4]. Similarly, the amplitude and phase of the quadrature vibration can also reflect the frequency split to achieve self-tuning [21]. By designing new tuning models, frequency split can be optimized [22]. The frequency split information can be obtained by applying the offset frequency [23] or phase [24] excitation signals to realize mode matching control. Besides, noise observation in the readout circuit also enables automatic frequency difference detection [25]. These methods reported improved bias instability and other metrics, but the influence of bias repeatability was not mentioned in the existing literature.

In this work, a novel milli-hertz frequency tuning framework is proposed to conduct reliable axi-symmetry gyroscopes with widely adopted amplitude modulation (AM) mode-matched operation mode. The features of this architecture are constituted as a precision frequency tracker and a mode reversal-based frequency tuning algorithm. The phase lock loop (PLL)-based precision frequency tracker is used to identify the resonant frequencies of two gyroscopic modes. The learning control algorithm works well for accurate tracking [26], [27], and an online learning controller (OLC) empowers the PLL to reach a mili-hertz noise level [28]. The mode reversal operation allows the frequency tracker to determine the frequency split and then utilize the electrostatic stiffness softening effect to eliminate the anisoelasticity.

The contributions of this article are summarized as follows.

1) The error mechanism and major error source of the axi-symmetry gyroscope bias repeatability are investigated and verified. The dynamic system model is investigated and the frequency split between the two gyroscopic modes turned out to be the main error contributor, especially if the gyroscope is with a high-Q design.

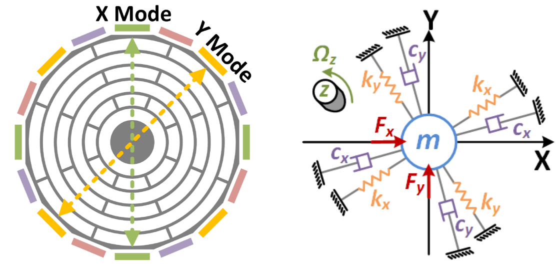

(a) (b)

Fig. 1. (a) Schematic diagram of electrodes distribution of axi-symmetry gyro. (b) Physical model of gyros is equivalent to a two-degree-of-freedom lumped parameter system in Cartesian coordinates.

2) A novel calibration architecture is proposed to eliminate the bias error source. It contains an OLC-PLL-based resonance frequency detector with a significant accuracy of milli-hertz level. Then, an automatic frequency split tuning (AFST) algorithm that cooperated with the mode reversal technology is designed for precision frequency split calibration.

3) The effectiveness of the proposed solution is experimentally verified and demonstrated as state-of-the-art results. The OLC-PLL detector and AFST algorithm are implemented with a micromachined silicon ring gyroscope. Experiments show that the proposed scheme achieves bias repeatability of 3.6°/h as a state-of-the-art record for an axi-symmetry gyroscope.

II. Operational Principle of a MEMS Gyroscope

A typical axi-symmetry gyroscope can be represented as in Fig. 1(a), which is designed as a multiring structure and utilizing $n = 2$ vibration mode as an example. The two degenerated gyroscopic modes (x and y) have an orientation angle of 45° for sake of electrostatic tuning functions [29]. The equivalent mechanical vibration model is shown in Fig. 1(b). The principal axes of x and y are considered orthogonal to each other, but there are stiffness and damping coupling mechanisms. The spring stiffness and damping coefficient of the two modes are also unbalanced in real practice because of the anisotropic material properties and fabrication imperfections [30].

Based on the abovementioned considerations, a practical dynamical model of a MEMS gyroscope can be established as

$$\begin{aligned} m\ddot{x} + c_x\dot{x} + k_x x + c_{yx}\dot{y} + k_{yx}y &= F_x - 2m\lambda\Omega_z\dot{y} \\ m\ddot{y} + c_y\dot{y} + k_y y + c_{xy}\dot{x} + k_{xy}x &= F_y + 2m\lambda\Omega_z\dot{x} \end{aligned} \tag{1}$$

where x and y are the displacements of the center mass in the two gyroscopic modes, m represents the effective mass, c_x and c_y are the damper coefficients, k_x and k_y are the spring coefficients of the two modes, F_x and F_y are defined as the electrostatic drive forces, the terms $2m\Omega_z\dot{y}$ and $2m\Omega_z\dot{x}$ are the Coriolis effect induced components, where Ω_z is the physical rotation in the Z axis that needs to be sensed, k_{xy} and k_{yx} are the stiffness coupling coefficients between each vibrating mode, c_{xy} and c_{yx} are the damper coupling coefficients. It is well known that the resonant frequencies of the two modes are defined as

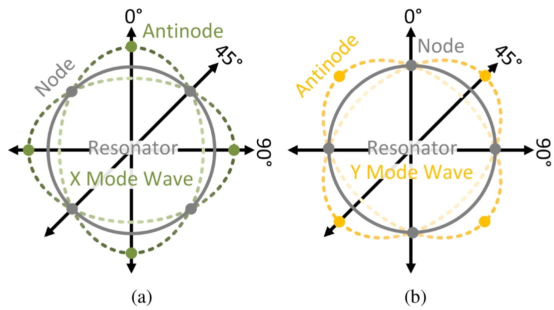

Fig. 2. Schematic diagram of the changing trend of gyro standing wave: (a) x mode (b) y mode.

$\omega_x = \sqrt{k_x/m}$ and $\omega_y = \sqrt{k_y/m}$. Thus, the damping coefficients also have alternative representations as $c_x/m = \omega_x Q_x$ and $c_y/m = \omega_y/Q_y$.

The cross coupling frequency ω_{xy} and ω_{yx}, and the cross coupling damper ρ_{xy} and ρ_{yx} are defined as follows:

$$\omega_{yx} = \omega_{xy} = \sqrt{\frac{k_{yx}}{m}}, \quad \rho_{yx} = \rho_{xy} = \frac{c_{xy}}{m}. \tag{2}$$

Under the classical operation architecture, $F_x = F_0 \sin(\omega t)$ and $F_y = 0$ would be applied to the gyroscope system (1). The frequency split is defined as $\Delta\omega = \omega_x - \omega_y$. If the artificial driven frequency $\omega \to \omega_x$, the solution to system (1) is given by

$$\begin{aligned} x(t) &= \frac{Q_x F_0}{m\omega_x^2}\cos(\omega_x t) \\ y(t) &= \frac{Q_x F_0}{m\omega_x^2}\frac{\left(2\lambda\Omega_z + \frac{\omega_{xy}}{Q_{xy}}\right)\cos(\omega_x t) - \frac{\omega_{xy}^2}{\omega_x^2} Q_x F_x \sin(\omega_x t + \phi)}{m\omega_x\sqrt{(2\Delta\omega)^2 + (\omega_y/Q_y)^2}} \\ \phi &= \arctan\left(\frac{\omega_y/Q_y}{2\Delta\omega}\right). \end{aligned} \tag{3}$$

The principles of $n = 2$ vibration mode shapes of the two gyro modes are shown in Fig. 2(a) and (b), respectively. By applying electrostatic excitation forces on the antinode electrodes, i.e., $F_x = F_0 \sin(\omega t)$ and $F_y = 0$, the resonant modes of the gyro vibrate accordingly. At this time, the excited amplitude can be detected on other antinode electrodes, and the signals in (3) are thus obtained.

The carrier frequency ω_x is typically between 5 kHz and 5 MHz. Meanwhile, the physical rotation is limited to the actually mounted system whose mechanical bandwidth is smaller than the 100-Hz range. Thus, the AM information is slow varying compared with the carrier signal, and can be demodulated into the baseband to give more room for signal processing and control.

III. Frequency Split Consequences and Precision Detection Method

A. Errors Induced by Frequency Splits

Theoretically, every coefficient in (1) is time-varying and has the potential to hurt the repeatability of MEMS gyroscopes. However, closed-loop control can effectively eliminate most of the parameter variations: automatic gain controllers can stabilize the output amplitude of $x(t)$ such that the term $Q_x F_0/m\omega_x^2$ is considered as time-invariant; PLLs can track the resonant frequency of x mode; quadrature nulling control utilize the spring softening effect to keep ω_{xy} at zero level.

The frequency split term $\Delta\omega$ is increasingly becoming an error contributor as the side effect of the popular symmetry high-Q designs. In (3), it can be observed that higher quality factors make the bias output level more sensitive to $\Delta\omega$. In addition, it starts to introduce the demodulation phase error. MEMS gyroscopes tend to be achieved higher Qs to improve the scale factor, so the frequency split tuning technique becomes more urgent.

B. OLC-PLL Based Precision Frequency Tracker

The major challenge of this architecture is the high accuracy and low-noise PLL controller. Selecting x as the nominal driven mode and defining ω as the PLL output. Then, the overall input frequency-output phase can be expressed as follows:

$$\psi = \arctan\left(\frac{\frac{\omega}{Q_x\omega_x}}{1 - \left(\frac{\omega}{\omega_x}\right)^2}\right) \tag{4}$$

where ψ is the phase shift between the excitation and output signals. During a small range around the resonant frequency such that $\omega \in [\omega_x - \epsilon, \omega_x + \epsilon]$, the relationship between the drive frequency and the detected phase can be considered as linear

$$\psi = \frac{Q_x}{2\pi\omega_x} f \tag{5}$$

where $f = \omega/2\pi$ represents the output of the excitation frequency.

As discussed before, there is a -90° phase shift between F_x and $x(t)$ as $\omega \to \omega_x$, which also indicates the precise resonant frequency of x mode. Similarly, ω_y can be determined in the same way if $F_x = 0$ and $F_y = F_0 \sin(\omega_t)$. The two modes can be excited in a periodical pattern to acquire $\Delta\omega$, which is compatible to the advanced *mode reversal* operation architecture. During the flipping processes, $\Delta\omega$ can be computed and eliminated through the frequency tuning electrodes. However, time delay effects and parameter variations make (5) be a dynamical process

$$\dot{\psi}(t) = -\gamma\psi(t) + \omega_\delta(t) + k_f f(t) \tag{6}$$

where $k_f = Q_x/2\pi\omega_x$; $\gamma > 1$ is the time delay coefficient that introduced by the front-end electronics and demodulation process; ω_δ is the equivalent disturbance that originated from the variation of ω_x which is typically assumed to be bounded, i.e., $|\omega_\delta| \leq \bar{\omega}_\delta$. It is remarkable that high-Q gyroscopes have very narrow resonance peaks (i.e., less than 0.1 Hz), so ω_δ with a few mHz level power will lead to a dramatic bias repeatability performance degradation.

Therefore, a high-precision PLL is highly desired. OLC has the ability to precisely track the resonance. Though the desired phase is -90°, we formulate this problem as stabilizing the origin with a coordinate transformation to simplify the theoretical derivations. The control algorithm is given by [31]

$$f(t) = k_1 f(t-\tau) + k_2 e(t) \tag{7}$$

where $e(t)$ is the instaneous controller to be designed; k_1 and k_2 are control parameters to be tuned; and τ is the learning interval. The main idea is to use a learning term $f(t-\tau)$ to follow the variation of ω_δ. The learning difference $\tilde{f}$ is defined as

$$\tilde{f} = f(t) - f(t-\tau). \tag{8}$$

Therefore, the control algorithm (7) can be expressed as

$$f(t) = k_1(f(t) - \tilde{f}) - k_2 e(t) \tag{9}$$

and can be simplified as

$$f(t) = -\kappa_1 e(t) - \kappa_2 \tilde{f} \tag{10}$$

where $\kappa_1 = k_2/(1-k_1)$, $\kappa_2 = k_1/(1-k_1)$. Note that, $\tilde{f}$ is limited in amplitude by the actuators, and therefore, the learning difference is naturally bounded i.e., $|\tilde{f}| \leq \bar{\tilde{f}}$.

Considering a proportional–integral (PI) controller as the instaneous one

$$e(t) = k_p \psi(t) + k_i \int_0^t \psi(s) ds \tag{11}$$

where k_p and k_i are control parameters. Select an intermediate state

$$z(t) = \int_0^t \psi(s) ds \tag{12}$$

and the instaneous controller (11) can be rewritten as

$$e(t) = k_p \psi(t) + k_i z(t). \tag{13}$$

C. Stability Analysis

Considering the phase lock control system given by (5) and (6), then by using the control law given by (7) and (11), the phase stabilization can be achieved, provided

$$0 < k_1 < 1, \quad k_2 > 0. \tag{14}$$

Consider the following Lyapunov function candidate:

$$V = \frac{1}{2}\psi(t)^2 + \frac{1}{2}k_f \kappa_1 k_i z(t)^2. \tag{15}$$

The derivative of V is

$$\dot{V} = \psi(t)\dot{\psi}(t) + k_f \kappa_1 k_i z(t) \dot{z}(t). \tag{16}$$

Substituting (6), (10), (12) and (13) into (16), it yields

$$\begin{aligned} \dot{V} =& -(\gamma + k_f \kappa_1 k_p)\psi(t)^2 + \omega_\delta(t)\psi(t) - k_f \kappa_2 \tilde{f} \psi(t) \\ \leq& -(\gamma + k_f \kappa_1 k_p)|\psi(t)|^2 + |\omega_\delta(t)||\psi(t)| + k_f \kappa_2 |\tilde{f}||\psi(t)| \\ \leq& -(\gamma + k_f \kappa_1 k_p - 1)|\psi(t)|^2 + \frac{1}{2}|\omega_\delta(t)|^2 + \frac{1}{2}k_f^2 \kappa_2^2 |\tilde{f}|^2 \\ \leq& -\mu|\psi(t)|^2 + \Pi \end{aligned} \tag{17}$$

where $\mu = \gamma + k_f \kappa_1 k_p - 1$, $\Pi = (1/2)|\omega_\delta(t)|^2 + (1/2){k_f}^2 {\kappa_2}^2 |\tilde{f}|^2$. Since $|\omega_\delta| \leq \bar{\omega_\delta}$ and $|\tilde{f}| \leq \bar{\tilde{f}}$, Π is bounded. If (14) is satisfied, one can easily verify $\mu > 0$. Thus, it is clear that when $|\psi(t)| > \sqrt{\Pi/\mu}$, $\dot{V} < 0$. This completes the proof. □

IV. Frequency Split Elimination Architecture

A. System architecture

The overall architecture of OLC-based automatic frequency tuning system for axi-symmetry gyroscope is shown in Fig. 3. Axi-symmetry electrodes are distributed around the gyroscope: yellow corresponds to the electrode of the y mode, green represents the electrode of the x mode, and purple represents the tuning electrode. Each pair of electrodes at 90° constitutes a differential input or output pair. Negative stiffness effects can be achieved by applying a dc voltage signal to the tuning electrodes at 22.5° from the main direction.

The stage 1 (S1) carriers are applied to the gyro ring to modulate the vibration signal to distinguish the capacitive feedthrough signal. In the pick-up circuits, the S1 carriers are differentially amplified and filtered by high-pass filters to remove the feedthrough signal, and then detected by diodes and low-pass filters (LPFs) to obtain the stage 2 (S2) carriers. The ADCs collect the carriers and send them to the multipliers and LPFs for the second demodulation to obtain the in-phase and quadrature-phase signals of the two modes of the gyro. The coordinate rotation digital computer (CORDIC) algorithm is exploited to resolve the phase of the two modes. The phase switching control operates according to the command of the mode switching algorithm.

According to the set phase value, the phase error is sent to the phase-locked loop based on the OLC algorithm to generate the frequency word. The numerically controlled oscillator (NCXO) receives the word and uses the accumulator and CORDIC algorithm to form the frequency signal, which is fed into the memory and the amplitude switching controller at the same time. The DACs thus generate acceptable S2 carriers for the gyro to excite the gyro via differential buffers. The AFST algorithm stores the frequencies of the two modes separately and uses a frequency split calculator to identify the frequency difference. The PI controller generates the corresponding tuning signal according to the frequency difference data to generate the gyro stiffness tuning voltage via the dc DAC. It is notable that this proposed calibration process would be performed in the gyro initialization phase. Once it is accomplished, it will not interfere with the normal gyro operation.

B. OLC-PLL Based Precision Frequency Tracking Algorithm

The premise of high-performance automatic frequency tuning is the high-precision identification of the resonant frequency of the gyro. The gyro phase-locked loop composed of the OLC algorithm for high-precision frequency characterization is shown in Algorithm 1. It first sets the initial frequency reference f_{ref} once, and then detects the current lock mode via LockState and extracts the corresponding phase value $\psi_x(t)$ or $\psi_y(t)$ for PI control. $E(t)$ is defined as the phase difference. The learning

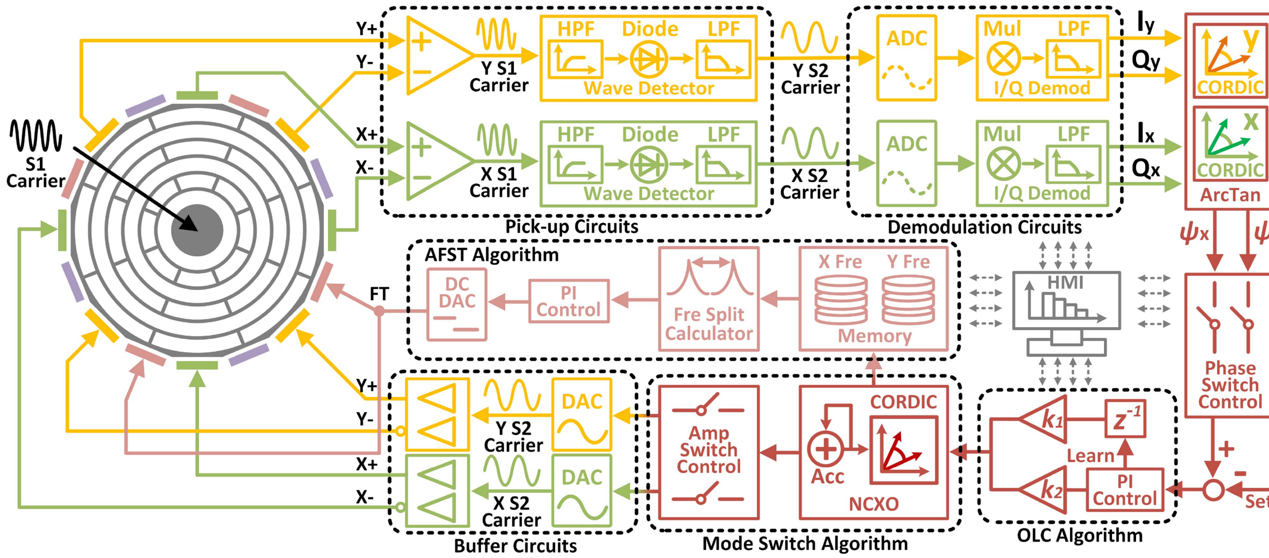

Fig. 3. The overall gyro system of automatic frequency split tuning architecture based on the OLC algorithm.

Algorithm 1: OLC-PLL.

Input: f_{ref}, $\psi_x(t)$, $\psi_y(t)$, k_i, k_p, $LockState$
Output: $f(t)$, $f(t-1)$, $e(t)$
if $LockState \neq False$ **then**
  if $f_{ref} \neq 0$ **then**
    $e(t-1) \leftarrow f_{ref}$
    $f_{ref} \leftarrow 0$
  end
  if $LockState = x$ **then**
    $\psi(t) \leftarrow \psi_x(t)$ `// Switch to x mode`
  end
  if $LockState = y$ **then**
    $\psi(t) \leftarrow \psi_y(t)$ `// Switch to y mode`
  end
  `// OLC algorithm`
  $E(t-1) \leftarrow E(t)$
  $E(t) \leftarrow \psi(t)$
  $e(t) \leftarrow e(t-1) + k_p * [E(t) - E(t-1)] + k_i * E(t)$
  $e(t-1) \leftarrow e(t)$
  $f(t) \leftarrow k_1 * f(t-1) + k_2 * e(t)$
  $f(t-1) \leftarrow f(t)$
end

interval τ is set to 1. The OLC algorithm continuously generates learning items based on the calculation results of PI control.

C. Mode Switch Algorithm

Time-sharing driving is the basis for the frequency identification of two gyro modes. Therefore, an efficient mode switching system is indispensable. As shown in Algorithm 2, tick timing is done by introducing t_{count}. A mode switch denoted by SwitchState is made every time the count value t_{count} reaches t_{sw}. Due to the asymmetry of the two gyro modes caused by the machining accuracy problem, the relevant parameters k_p, k_i are also reloaded with specified k_{p-x}, k_{i-x} or k_{p-y}, k_{i-y}

Algorithm 2: Gyro Mode Switch.

Input: t_{sw}, k_{p-x}, k_{i-x}, k_{p-y}, k_{i-y}, $LockState$, $SwitchState$
Output: $E(t)$, $E(t-1)$, k_i, k_p, $E_{\Delta\omega}(t)$, $E_{\Delta\omega}(t-1)$, t_{count}
if $SwitchState = True$ **then**
  $t_{count}++$
  if $t_{count} = t_{sw}$ **then**
    $t_{count} \leftarrow 0$
    $E(t) \leftarrow 0$
    $E(t-1) \leftarrow 0$
    $E_{\Delta\omega}(t) \leftarrow 0$
    $E_{\Delta\omega}(t-1) \leftarrow 0$
    if $LockState = x$ **then**
      $k_p \leftarrow k_{p-y}$
      $k_i \leftarrow k_{i-y}$
      $LockState \leftarrow y$ `// Switch to y`
    end
    if $LockState = y$ **then**
      $k_p \leftarrow k_{p-x}$
      $k_i \leftarrow k_{i-x}$
      $LockState \leftarrow x$ `// Switch to x`
    end
  end
end

when switching. At the same time, the historical data of the control loop, such as error $E(t)$ and $E(t-1)$, is cleared. Error parameters $E_{\Delta\omega}(t)$, $E_{\Delta\omega}(t-1)$ in AFST control are no longer applicable because of time-varying factors and are also cleared.

D. AFST Algorithm

The AFST algorithm, including the aforementioned two key algorithms, is shown in Algorithm 3. In the early stage of gyro switching, the resonant frequency is not stable during the settling

Algorithm 3: AFST.

Input: t_{th}, v_{ref}, $k_{p-\Delta\omega}$, $k_{i-\Delta\omega}$
Output: $E_{\Delta\omega}(t)$, $v(t)$
while *True* **do**
  Algorithm 1
  Algorithm 2
  `// Calculate frequency split`
  if $SwitchState = True$ **then**
    if $t_{th} - 1 \leq t_{count} < t_{sw} - 1$ **then**
      $f_{sum} \leftarrow f_{sum} + \dfrac{f(t)}{t_{sw} - t_{th}}$
      $AFSTState \leftarrow True$
    end
    if $t_{count} = t_{sw} - 1$ **then**
      $AFSTState \leftarrow False$
      $f_{avg} \leftarrow f_{sum}$
      $f_{sum} \leftarrow 0$
    end
  end
  `// Enable frequency tuning`
  if $AFSTState = True \ \& \ LockState = x$ **then**
    if $v_{ref} \neq 0$ **then**
      $v(t-1) \leftarrow v_{ref}$
      $v_{ref} \leftarrow 0$
    end
    $E_{\Delta\omega}(t-1) \leftarrow E_{\Delta\omega}(t)$
    $E_{\Delta\omega}(t) \leftarrow f(t) - f_{avg}$
    $v(t) \leftarrow v(t-1) + k_{p-\Delta\omega} * [E_{\Delta\omega}(t) - E_{\Delta\omega}(t-1)] + k_{i-\Delta\omega} * E_{\Delta\omega}(t)$
    $v(t-1) \leftarrow v(t)$
  end
end

time stage. Therefore, the threshold time t_{th} is set to ensure the accuracy of frequency identification and the reliability of AFST control. Within a specified t_{th}, the frequencies of the respective modes are calculated through f_{sum} and f_{avg}, then the AFST control denoted by AFSTState is turned-ON. Terms of $k_{p-\Delta\omega}$ and $k_{i-\Delta\omega}$ are the control parameters for the frequency tuning PI control.

In practice, only one mode needs to be stiffness tuned to fix the frequency difference. The x mode is chosen here as an example, and its initial set tuning voltage is v_{ref}. When driving the x mode, the frequency difference $E_{\Delta\omega}(t)$ is calculated according to the y mode average frequency obtained last time as an error to generate the tuning signal $v(t)$. It is input to the corresponding gyro electrode through the dc DAC to complete the frequency difference closed-loop tuning.

V. Experiment Validation

A. Hardware Implementation

Fig. 4 shows the implemented prototype of the proposed calibration scheme. The high-frequency signal generator provides the S1 carrier for the microgyroscope, and the front-end vibration pick-up circuits cooperate with the detector circuits to extract the S2 carriers. A field programmable gate array

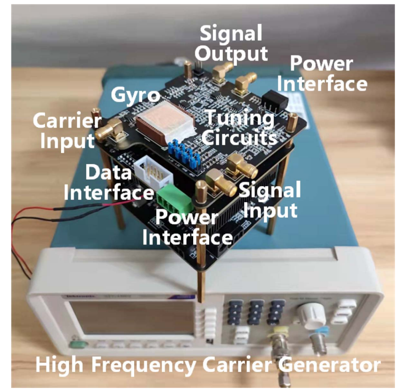

Fig. 4. Prototype of the microgyro frequency tuning system.

(FPGA) with high-speed signal processing capability is used to process S2 carriers at the kHz level. Digital signal processes, such as demodulation, phase detector, NCXO, and Algorithm 1–Algorithm 3, are implemented in this digital domain. It is noted that the Xilinx ZYNQ FPGA chip has both traditional high-speed parallel parts and the embedded ARM core. The AFST algorithm works at the baseband signal level and is implemented by register operations in the ARM core. The tuning signal is provided by a dc DAC to corresponding gyro electrodes to adjust the resonator stiffness for frequency tuning. At the same time, the frequency calculated by the OLC-based PLL in the ARM core is used by the FPGA as the carrier frequency to generate the S2 carriers to excite the gyro. Finally, the ARM core communicates with the human–machine interface through FPGA to realize real-time data reception and transmission.

A ring-type axi-symmetry microgyroscope with a resonant frequency of $\sim$5.3 kHz is chosen, which means that the S2 carrier is $\sim$5 kHz. In order to ensure the normal operation of the wave detector, a 1-MHz signal that is far away from the S2 carrier in the frequency domain is selected as the S1 carrier. The operating cycle of the ARM core is set to 1 ms, that is, the learning interval τ is 1 ms.

B. OLC-PLL Preliminary Test

The feasibility of the proposed OLC-PLL frequency tracker is first evaluated. The OLC control parameters are adjusted according to (14). The adjustment of PI control parameters refers to the Ziegler-Nichols method. The data of the phase-locking process based on OLC is shown in Fig. 5. Terms of $e(t)$, $f(t-1)$ and $f(t)$ in (7) show the process of online learning. The gray line is the calculated result of the PI control, which is accompanied by large noise and overshoot. The light blue line and the orange line are the online learning term and the final control input, respectively, which make the control instructions more accurate through continuous learning from previous experience in $e(t)$. Performances, such as overshoot and noise, are improved, thereby improving the accuracy of resonant frequency characterization. The phase error curve shows the effectiveness of the OLC phase lock operation, the phase difference is eventually settled to zero.

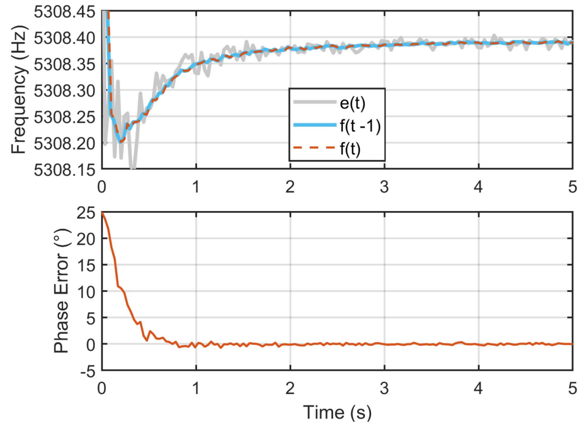

Fig. 5. Control input and gyro phase error changes after the phase-locked loop is turned-ON.

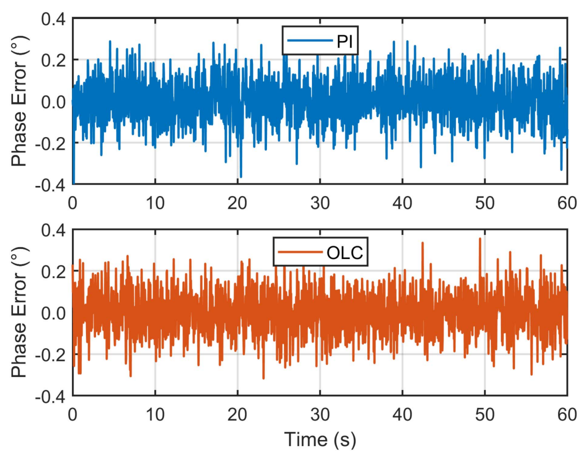

Fig. 6. Comparison of phase errors in phase-locked loops.

In a nutshell, online learning in the phase-locking process only relies on its own experience, which means that it can achieve good results without the need for adaptation and observer tools. This determines the simplicity of its implementation and parameter tuning.

C. Precision Frequency Detection Experiment

The performance is compared by identifying the frequency through the PLL using the PI and OLC controllers, respectively. For fairness, the k_p and k_i parameters in PI and OLC are set to be the same. From the phase locking results shown in Fig. 6, both methods can control the phase error within $\pm$ 0.4°, which are effective and acceptable performance. That is to say, the phase-locking effect of the gyro can be effectively guaranteed under both methods.

The frequency identification comparison is shown in Fig. 7. The frequency identification accuracy of PI can only reach the level of 30 mHz, and the OLC can reach the level of about 3 mHz, which reflects an order of magnitude improvement. For the first time, the resonant frequency identification of the micro-gyroscope has reached the mHz level, which is a state-of-the-art achievement in breaking performance bottlenecks.

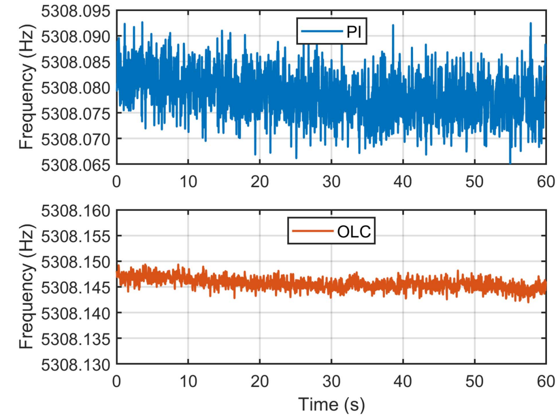

Fig. 7. Comparison of phase-locked loop frequency characterization accuracy.

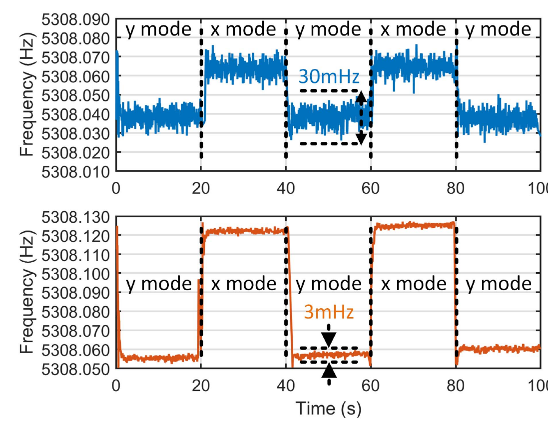

Fig. 8. Comparison of frequency characterization accuracy with gyro mode switching.

As illustrated in Fig. 8, t_{sw} is set to 20 s for the gyro mode switching test in the unmatched state. Note that tuning voltages and axis scales are set to be the same to reflect fairness. The change in actual frequency in both results is due to environment-induced drift. Both methods can effectively identify the resonant frequencies of the two modes of the gyro, and the accuracy of the OLC is about an order of magnitude higher, which is consistent with the results shown in Fig. 7.

To sum up, OLC can ensure the real-time performance of closed-loop control to cope with the frequency drift by using the calculation results of the PI controller at this moment. Meanwhile, OLC also continuously learns the last frequency information, and the relevant lessons learned from it are applied to control decisions for weakening drastic changes to suppress noise.

D. Gyro Bias Repeatability Test

Figs. 9 and 10 show the tuning voltage and frequency difference changes during the operation of the AFST algorithm, respectively. t_{sw} is set to 3 s, that is, frequency tuning calibration is done every 6 s. Both methods can suppress the frequency difference within a reasonable range during the second calibration. After this, the PI can only maintain the tuning voltage

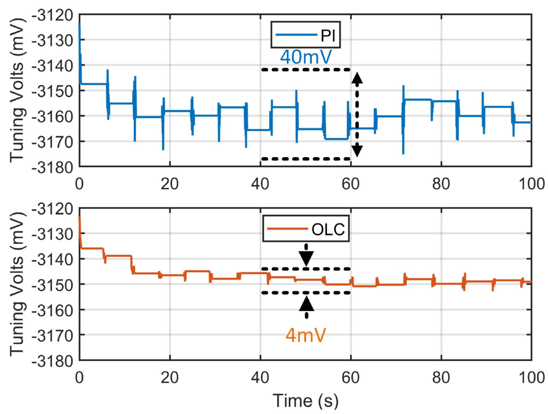

Fig. 9. Tuning voltage comparison after auto frequency split tuning is turned-ON.

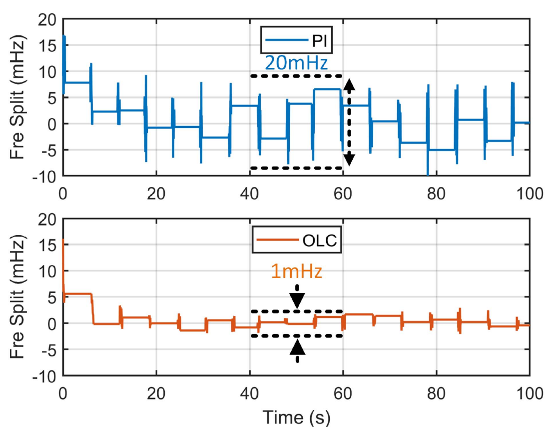

Fig. 10. Frequency difference comparison after auto frequency split tuning is enabled.

accuracy within 40 mV, while the OLC can reach ~4 mV, which means our proposed method shows ~ 10× control accuracy. Consequently, PI can only suppress frequency split within 20 mHz, while OLC-PLL can reduce it to 1-mHz level.

The most important evaluation of this work is the turn-ON to turn-ON bias repeatability experiment. For each run, the gyro system is turned-OFFand on again without any temperature control, then the average value of the zero rate output signal over 1 s is collected as the bias data. Then the systems will be entirely turned-OFF for 30-min cool down and repeat the turn-ON and data recording again. Three groups of bias repeatability data were collected, which are shown in Fig. 11. There are no further data selection operations or filtering in the six consecutive data points, and they are all raw data without algorithmic compensation.

The control group utilizes a conventional stored look-up table approach to compensate the bias variations. This method is unfortunately failed with bias repeatability exceeding 5000°/h, because this black box is difficult to adapt to new environments. Then our proposed scheme with a PI-PLL frequency tracker is tested to provide a comparison. Since this combination can reduce the frequency split to a 10-mHz level, the bias repeatability is also improved to a 100°h level. Finally, our fully functioning architecture with OLC-PLL conducts the best results with a maximum–minimum difference of 10°h. To exclude the random

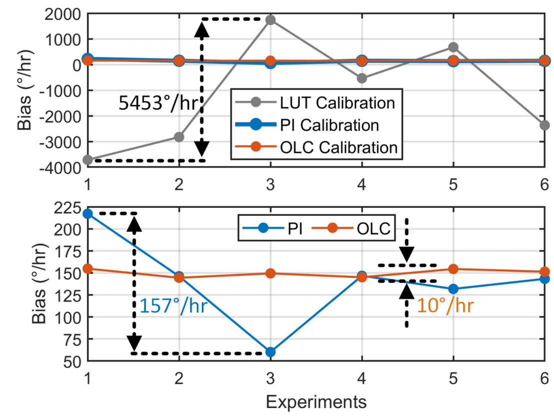

Fig. 11. Comparison of microgyro system bias repeatability.

errors, the mean absolute error (MAE) metric is introduced to evaluate gyro bias repeatability. MAE has the ability to reflect the level of mean deviation. The results of the three groups are 1798°h, 30°h, and 3.6°h, respectively, where our proposed method is showing a state-of-the-art axi-symmetry gyroscope bias repeatability performance.

In summary, our proposed architecture can effectively improve the bias repeatability of axi-symmetry micromachined gyroscopes by eliminating the inherent error source. The OLC-PLL-based frequency tracker can reach a milli-hertz precision to ensure the mode reversal and AFST to eliminate the frequency splits accurately.

VI. Conclusion

In this article, we proposed and demonstrated an ultraprecise frequency tuning solution to address the turn-ON to turn-ON bias repeatability issue for axi-symmetry micro gyroscopes. The dynamical model was first analyzed to demonstrate the error mechanism that frequency split was the key contributor. An OLC enforced PLL was then presented to characterize the splits, and full auto frequency tuning architecture was developed. The experimental results show that the frequency split tuning accuracy was at 1-mHz level and the bias repeatability was 3.6°/h that both were state of the art. It has the potential to be expanded in a broad kinds of MEMS gyroscopes to enhance their reliability.

References

[1] X. Shao, Y. Shi, W. Zhang, and H. Cao, "Neurodynamic approximation-based quantized control with improved transient performances for micro-electromechanical system gyroscopes: Theory and experimental results," *IEEE Trans. Ind. Electron.*, vol. 68, no. 10, pp. 9972–9983, Oct. 2021.

[2] X. Zhou et al., "Decaying time constant enhanced MEMS disk resonator for high precision gyroscopic application," *IEEE/ASME Trans. Mechatron.*, vol. 23, no. 1, pp. 452–458, Feb. 2018.

[3] S. Yang, Z. Wu, W. Jia, and G. Wu, "Ultra-low relative frequency split piezoelectric ring resonator designed for high-performance mode-matching gyroscope," *J. Microelectromech. Syst.*, vol. 31, no. 1, pp. 6–8, 2021, doi: 10.1109/JMEMS.2021.3132371.

[4] C. Li et al., "An FPGA-based interface system for high-frequency bulk-acoustic-wave microgyroscopes with in-run automatic mode-matching," *IEEE Trans. Instrum. Meas.*, vol. 69, no. 4, pp. 1783–1793, Apr. 2020.

[5] Y. Zhang et al., "A rate-integrating honeycomb disk resonator gyroscope with 0.038°/h bias instability and 7000°/s measurement range," *IEEE Electron Device Lett.*, vol. 42, no. 4, pp. 581–584, Apr. 2021.

[6] J. Sun et al., "0.79 ppm scale-factor nonlinearity whole-angle microshell gyroscope realized by real-time calibration of capacitive displacement detection," *Microsystems Nanoeng.*, vol. 7, no. 1, pp. 1–11, 2021.

[7] J. Cui and Q. Zhao, "A high performance tactical-grade monolithic horizontal dual-axis MEMS gyroscope with off-plane coupling suppression silicon gratings," *IEEE Trans. Ind. Electron.*, vol. 69, no. 11, pp. 11765–11773, Nov. 2022, doi: 10.1109/TIE.2021.3127036.

[8] J. Giner, D. Maeda, K. Ono, A. M. Shkel, and T. Sekiguchi, "MEMS gyroscope with concentrated springs suspensions demonstrating single digit frequency split and temperature robustness," *J. Microelectromech. Syst.*, vol. 28, no. 1, pp. 25–35, 2018.

[9] Q. Li et al., "Nonlinearity reduction in disk resonator gyroscopes based on the vibration amplification effect," *IEEE Trans. Ind. Electron.*, vol. 67, no. 8, pp. 6946–6954, Aug. 2020.

[10] J. Cho et al., "High-Q navigation-grade fused-silica micro birdbath resonator gyroscope," in *Proc. IEEE Sensors*, 2021, pp. 1–4.

[11] B. Johnson et al., "Development of a navigation-grade MEMS IMU," in *Proc. IEEE Int. Symp. Inertial Sensors Syst.*, 2021, pp. 1–4.

[12] G. Langfelder, M. Bestetti, and M. Gadola, "Silicon MEMS inertial sensors evolution over a quarter century," *J. Micromech. Microeng.*, vol. 31, no. 8, 2021, Art. no. 084002.

[13] X. Zhou et al., "Dynamic modulation of modal coupling in microelectromechanical gyroscopic ring resonators," *Nat. Commun.*, vol. 10, no. 1, pp. 1–9, 2019.

[14] X. Tong, M. Chen, and F. Yang, "Robust hybrid attitude and gyro-bias observer on quaternions," *IEEE Trans. Ind. Electron.*, vol. 69, no. 8, pp. 8545–8553, Aug. 2022, doi: 10.1109/TIE.2021.3108713.

[15] D. Endean et al., "Near-navigation grade tuning fork MEMS gyroscope," in *Proc. IEEE Int. Symp. Inertial Sensors Syst.*, 2019, pp. 1–4.

[16] M. Gadola, A. Buffoli, M. Sansa, A. Berthelot, P. Robert, and G. Langfelder, "1.3 mm 2 nav-grade NEMS-based gyroscope," *J. Microelectromech. Syst.*, vol. 30, no. 4, pp. 513–520, 2021.

[17] A. D. Challoner, J. Daniel, P. Bond, J. Beitia, and R. K. Li, "A new IMU with a digitally controlled PZT CVG," in *Proc. IEEE/ION Position, Location Navigation Symp.*, 2018, pp. 1–6.

[18] I. Prikhodko, J. Geen, C. Merritt, and S. Zhang, "Vibration immune, long-term stable and low noise synchronized mass MEMS gyroscope," in *Proc. IEEE Int. Symp. Inertial Sensors Syst.*, 2021, pp. 1–4.

[19] H. Cao, Q. Cai, Y. Zhang, C. Shen, Y. Shi, and J. Liu, "Design, fabrication, and experiment of a decoupled multi-frame vibration MEMS gyroscope," *IEEE Sensors J.*, vol. 21, no. 18, pp. 19815–19824, Sep. 2021.

[20] I. P. Prikhodko et al., "Mode-matched MEMS coriolis vibratory gyroscopes: Myth or reality?," in *Proc. IEEE/ION Position, Location Navigation Symp.*, 2016, pp. 1–4.

[21] Z. Hu and B. J. Gallacher, "Precision mode tuning towards a low angle drift mems rate integrating gyroscope," *Mechatronics*, vol. 56, pp. 306–317, 2018.

[22] X. Ren, X. Zhou, Y. Tao, Q. Li, X. Wu, and D. Xiao, "Radially pleated disk resonator for gyroscopic application," *J. Microelectromech. Syst.*, vol. 30, no. 6, pp. 825–835, 2021.

[23] Y. Zhou, J. Ren, M. Liu, T. Zhou, and Y. Su, "An in-run automatic mode-matching method for N= 3 MEMS disk resonator gyroscope," *IEEE Sensors J.*, vol. 21, no. 24, pp. 27601–27611, Dec. 2021.

[24] F. Bu, D. Xu, H. Zhao, B. Fan, and M. Cheng, "MEMS gyroscope automatic real-time mode-matching method based on phase-shifted 45° additional force demodulation," *Sensors*, vol. 18, no. 9, 2018, Art. no. 3001.

[25] M. Marx, X. Cuignet, S. Nessler, D. De Dorigo, and Y. Manoli, "An automatic MEMS gyroscope mode matching circuit based on noise observation," *IEEE Trans. Circuits Syst. II: Exp. Briefs*, vol. 66, no. 5, pp. 743–747, May 2019.

[26] C. Zhang, J. Wu, C. K. Ahn, Z. Fei, and C. Wei, "Learning observer and performance tuning-based robust consensus policy for multiagent systems," *IEEE Syst. J.*, vol. 16, no. 1, pp. 431–439, Mar. 2022, doi: 10.1109/JSYST.2020.3047644.

[27] C. Zhang, C. K. Ahn, J. Wu, W. He, Y. Jiang, and M. Liu, "Robustification of learning observers to uncertainty identification via time-varying learning intensity," *IEEE Trans. Circuits Syst. II: Exp. Briefs*, vol. 69, no. 3, pp. 1292–1296, Mar. 2022, doi: 10.1109/TCSII.2021.3107161.

[28] C. Zhang, C. K. Ahn, J. Wu, and W. He, "Online-learning control with weakened saturation response to attitude tracking: A variable learning intensity approach," *Aerosp. Sci. Technol.*, vol. 117, 2021, Art. no. 106981.

[29] H. Wang, H. Quan, J. Zhou, L. Zhang, J. Xie, and H. Chang, "A wafer-level vacuum packaged MEMS disk resonator gyroscope with 0.42°/h bias instability within °/s full scale," *IEEE Trans. Ind. Electron.*, vol. 69, no. 5, pp. 5304–5313, May 2022.

[30] M. Parajuli, G. Sobreviela, M. Pandit, H. Zhang, and A. A. Seshia, "Sub-deg-per-hour edge-anchored bulk acoustic wave micromachined disk gyroscope," *J. Microelectromech. Syst.*, vol. 30, no. 6, pp. 836–842, 2021.

[31] C. Zhang, B. Xiao, J. Wu, and B. Li, "On low-complexity control design to spacecraft attitude stabilization: An online-learning approach," *Aerosp. Sci. Technol.*, vol. 110, 2021, Art. no. 106441.

Chong Li (Member, IEEE) received the B.E. degree in automation and M.E. degree in control theory and control engineering from the Ocean University of China, Qingdao, China, in 2009 and 2012, respectively, and the Ph.D. degree in mechanical engineering from Auburn University, Auburn, AL, USA, in 2016.

He is currently an Associate Professor with the Department of Automation and Measurement, Ocean University of China. From 2016 to 2018, he was a Postdoctoral Research Fellow with the Integrated MEMS Laboratory (IMEMS), Center for MEMS and Microsystems Technologies (CMMT), Georgia Tech. His research interests include MEMS, control systems, high-performance computing, and artificial intelligence.

Yuchen Wang (Student Member, IEEE) received the B.E. degree in automation from the National Scholarship, Qingdao University of Science and Technology, Qingdao, China, in 2019.

He is currently working toward the M.E. degree in control theory and control engineering with the Ocean University of China, Qingdao, China, with the National Scholarship. He has authored or coauthored more than 10 patents. His research interests include MEMS, resonator interface electronics, measurement and control systems, and calibration technology.

Choon Ki Ahn (Senior Member, IEEE) received the B.S. and M.S. degrees in control engineering from the School of Electrical Engineering, Korea University, Seoul, Korea, in 2000 and 2002, respectively, and the Ph.D. degree in control engineering from the School of Electrical Engineering and Computer Science, Seoul National University, Seoul, Korea, in 2006.

He is currently a *Crimson Professor of Excellence* with the College of Engineering and a Full Professor with the School of Electrical Engineering, Korea University, Seoul, Korea.

Dr. Ahn was the recipient of the Early Career Research Award of Korea University in 2015. In 2016, he was ranked #1 in Electrical/Electronic Engineering among Korean young professors based on research quality. In 2017, he received the *Presidential Young Scientist Award* from the President of South Korea. In 2020, he received the Outstanding Associate Editor Award for *IEEE Transactions on Neural Networks and Learning Systems*. In 2021, he received the Best Associate Editor Award for *IEEE Transactions on Systems, Man, and Cybernetics: Systems*. In 2019–2022, he received the Research Excellence Award from Korea University (Top 3% Professor of Korea University in Research). He has been a Senior Editor of IEEE TRANSACTIONS ON NEURAL NETWORKS AND LEARNING SYSTEMS, a Senior Associate Editor of *IEEE Systems Journal*, and an Associate Editor for IEEE TRANSACTIONS ON FUZZY SYSTEMS*;* IEEE TRANSACTIONS ON SYSTEMS, MAN, AND CYBERNETICS: SYSTEMS*;* IEEE TRANSACTIONS ON AUTOMATION SCIENCE AND ENGINEERING*;* IEEE TRANSACTIONS ON INTELLIGENT TRANSPORTATION SYSTEMS*;* IEEE TRANSACTIONS ON CIRCUITS AND SYSTEMS I: REGULAR PAPERS*; IEEE Systems, Man, and Cybernetics Magazine; Nonlinear Dynamics; Aerospace Science and Technology; and other flagship journals*. He was also the recipient of the Highly Cited Researcher Award in Engineering by Clarivate Analytics (formerly, Thomson Reuters).

Chengxi Zhang (Member, IEEE) was born in Shandong, China, in Febuary 1990. He received the B.S. and M.S. degrees in microelectronics and solid-state electronics from the Harbin Institute of Technology, Shenzhen, China, in 2012 and 2015, respectively, and the Ph.D. degree in control science and engineering from Shanghai Jiao Tong University, China, in 2019.

He is currently a Postdoctoral Fellow with the School of Electronic and Information Engineering, Harbin Institute of Technology, Shenzhen Campus, China. His research interests include embedded system software and hardware design, information fusion, and control theory.

Bo Wang (Graduate Student Member, IEEE) received the M.S. degree in control theory and engineering from the University of Chinese Academy of Sciences, Beijing, China, in 2018.

He is currently a Ph.D. degree in dynamic systems and control with the Department of Mechanical Engineering, Villanova University, USA. His research interests include nonlinear control theory (robust, adaptive, passive, etc.), underactuated systems, nonholonomic systems, networked control systems, and robotics.